

High-order harmonic generation in imperfect crystals

Chuan Yu, Kenneth K. Hansen, and Lars Bojer Madsen

Department of Physics and Astronomy, Aarhus University, 8000 Aarhus C, Denmark

(Received 6 March 2019; published 13 June 2019)

High-order harmonic generation (HHG) in imperfect crystals, where the disorder is modeled by random shifts of the ionic positions, is studied using time-dependent density-functional theory. When irradiated by midinfrared laser pulses, the disorder-free system produces HHG spectra with two plateaus. Compared with the disorder-free system, disordered systems are found to emit suppressed harmonics in the first plateau region and enhanced harmonics in the second plateau region. The suppression of harmonics in the first plateau becomes less pronounced when decreasing the displacement of the nuclei, while the enhancement in the second plateau region is insensitive to the range of the ionic displacement. We have confirmed these findings for many different disordered sample systems and for different laser field strengths. The increase of the HHG signals in the second plateau region is proposed to stem from a change of the dynamics in the system, evidenced by the transition matrix elements between the field-free Kohn-Sham orbitals. In addition, a time-frequency profile of HHG spectra shows that the emission of harmonics is less regular in the time domain for a disordered system than for the disorder-free system.

DOI: [10.1103/PhysRevA.99.063408](https://doi.org/10.1103/PhysRevA.99.063408)**I. INTRODUCTION**

High-order harmonic generation (HHG) in gases [1,2] is one of the fundamental strong-field phenomena in laser-matter interactions. It allows for production of subfemtosecond laser pulses, with which ultrafast dynamics in matter can be explored on femto- and attosecond timescales [3]. Recently, HHG in solids was demonstrated [4–9] with potential applications as a novel XUV light source and for probing ultrafast dynamics in condensed-matter systems [10]. High-order harmonic generation and ultrafast processes in bulk and nanostructured materials attract considerable theoretical interest in this new research area where strong-field laser physics meets condensed matter. It has been demonstrated that some strong-field concepts, such as the three-step model for HHG [11], can be generalized to describe laser-induced processes in solids when the band structure is taken into account [12,13].

In most of the theoretical studies so far, the solid-state system interacting with the laser field is treated as a perfect crystal with a periodic lattice structure. Theoretical models for HHG in a solid with some form of disorder have only been considered very recently, e.g., for investigating effects of doping-type impurities [14,15] and for simulating a two-band tight-binding model of Anderson disorder [16]. Recent experiments have demonstrated HHG in amorphous solids [17,18] and liquids [19], implying that a perfect periodic lattice is not a stringent requirement for HHG in condensed-matter systems. Consequently, theoretical research on HHG in an imperfect crystal is becoming very relevant. It is natural to ask how the HHG spectral features will be modified by breaking the lattice periodicity. A complete answer to this question, however, is not yet available. As will be shown in this paper, disorder has an impact on the harmonic yield not only in the

first plateau region, but also in the higher-order region beyond the first cutoff, which cannot be described by the two-band model used previously [16]. To further explore the spectral features of HHG in an imperfect crystal, in this work we perform self-consistent simulations of HHG in disordered model systems, which could be relevant also to HHG in amorphous materials. Since very little has been done in this direction, we find it interesting and relevant to investigate how disorder affects the HHG spectra in a general setting. So in this work we study the effects of deviation away from perfect lattice order by introducing random shifts of the nuclear positions instead of modeling a particular type of lattice defects such as impurities or vacancies.

Note that breaking the lattice periodicity increases the theoretical complexity, since Bloch's theorem becomes inapplicable and one cannot simply use periodic boundary conditions in calculations. Previous theoretical investigations on HHG in solids are typically based on the semiconductor Bloch equations [12,20–23] or the time-dependent Schrödinger equation in single-active-electron (SAE) models [24–31]. In pursuit of going beyond the SAE models, there are also theoretical works that employ many-electron approaches such as the time-dependent density-functional theory (TDDFT) [32–37] and the time-dependent Hartree-Fock theory [38]. In this work we use a TDDFT model as in Refs. [15,35–37,39,40], which accounts for many interacting electrons, at least on a mean-field level. As will be shown below, this approach allows us to model an imperfect crystal in a straightforward manner, without making additional assumptions.

This paper is organized as follows. In Sec. II we describe the theoretical model and methods used in this work. The results of the calculations are presented and discussed in Sec. III. We conclude with a brief summary. Atomic units (a.u.) are used throughout unless stated otherwise.

II. THEORETICAL MODEL AND METHODS

In order to study the generic effects of disorder in HHG processes, the first step is to set up a model that can qualitatively represent a condensed-matter system with typical band structures. Following previous works [15,35–37], we consider a finite system so large that it behaves like a solid. Let us first introduce the model for a perfect crystal with one of the crystal directions along the linear polarization of the laser field. This model will be used for comparison with the disordered systems in our discussion in Sec. III. To model a disorder-free crystal, we consider a linear chain of N equally charged nuclei with a separation a and located at $x_j = [j - (N + 1)/2]a$ ($j = 1, \dots, N$). The ionic potential reads

$$v_{\text{ion}}(x) = - \sum_{j=1}^N \frac{Z}{\sqrt{(x - x_j)^2 + \epsilon}}, \quad (1)$$

where Z is the charge of each ion and ϵ is a softening parameter which smoothens the Coulomb singularity in a one-dimensional (1D) treatment. In this work we set $N = 200$, $Z = 2$, $\epsilon = 2$, and $a = 4$. This model, similar to the system A in Ref. [35], can qualitatively represent a crystal with a fully occupied valence band, and we will return to the corresponding band structures below.

The disorder of an imperfect crystal considered in our model is described by random shifts of the ionic locations,

$$x_j \rightarrow \tilde{x}_j = x_j + r_j \delta, \quad (2)$$

where r_j ($j = 1, \dots, N$) are random numbers uniformly distributed within $[-1, 1]$ and δ ($< a/2$) is a parameter for specifying the range of the random shifts. All the considered systems (with and without disorder) are charge and spin neutral. Thus the number of electrons with opposite spin is $N_{\downarrow} = N_{\uparrow} = N$ for the present case with $Z = 2$.

We treat the field-free electronic states for our model systems with density-functional theory (DFT). In the Kohn-Sham (KS) scheme, we find a set of KS orbitals determined by

$$\left\{ -\frac{1}{2} \frac{\partial^2}{\partial x^2} + v_{\text{KS}}[\{n_{\sigma}\}](x) \right\} \varphi_{j,\sigma}(x) = \varepsilon_{j,\sigma} \varphi_{j,\sigma}(x), \quad (3)$$

with the static KS potential

$$v_{\text{KS}}[\{n_{\sigma}\}](x) = v_{\text{ion}}(x) + v_{\text{H}}[n](x) + v_{\text{xc}}[\{n_{\sigma}\}](x). \quad (4)$$

The Hartree potential reads

$$v_{\text{H}}[n](x) = \int dx' \frac{n(x')}{\sqrt{(x - x')^2 + \epsilon}} \quad (5)$$

and the exchange-correlation potential is treated in a local spin-density approximation (LSDA)

$$v_{\text{xc}}[n_{\sigma}](x) \simeq v_{\text{x}}[n_{\sigma}](x) = - \left[\frac{6}{\pi} n_{\sigma}(x) \right]^{1/3}. \quad (6)$$

The spin densities are $n_{\sigma}(x) = \sum_{j=1}^{N_{\sigma}} |\varphi_{j,\sigma}(x)|^2$ for spin $\sigma = \downarrow, \uparrow$ and the total density is $n(x) = \sum_{\sigma=\downarrow,\uparrow} n_{\sigma}(x)$. Here we use the LSDA exchange potential for the 3D electron gas because our model aims to simulate HHG from a 3D system

driven by linearly polarized laser rather than to solve an exact 1D system. A previous study [35] showed that this approach captures the main features of HHG in bulk solids.

For the driving laser pulse linearly polarized along the x axis, we use the vector potential

$$A(t) = A_0 \sin^2 \left(\frac{\omega_0 t}{2N_c} \right) \sin(\omega_0 t) \quad (0 \leq t \leq 2\pi N_c / \omega_0), \quad (7)$$

with ω_0 the angular frequency (photon energy) and N_c the number of cycles. The laser-driven many-electron system is governed by the time-dependent KS equations

$$i \frac{\partial}{\partial t} \varphi_{j,\sigma}(x, t) = \left\{ -\frac{1}{2} \frac{\partial^2}{\partial x^2} - iA(t) \frac{\partial}{\partial x} + \tilde{v}_{\text{KS}}[\{n_{\sigma}\}](x, t) \right\} \varphi_{j,\sigma}(x, t), \quad (8)$$

where the KS potential

$$\tilde{v}_{\text{KS}}[\{n_{\sigma}\}](x, t) = v_{\text{ion}}(x) + v_{\text{H}}[n](x, t) + v_{\text{xc}}[\{n_{\sigma}\}](x, t) \quad (9)$$

is time dependent due to the time dependence of $n(x, t)$ and $n_{\sigma}(x, t)$.

We propagate the time-dependent KS orbitals using the Crank-Nicolson approach with a predictor-corrector step for updating the KS potential [41,42]. The initial conditions for the TDDFT calculations, i.e., the field-free ground-state KS orbitals, are found via imaginary-time propagation with orthogonalization in each time step [41]. Using the ground-state occupied KS orbitals as the initial state, we perform TDDFT calculations for the systems interacting with an eight-cycle laser pulse of frequency $\omega_0 = 0.015$ corresponding to a wavelength of approximately $3 \mu\text{m}$. The numerical calculations are performed on an equidistant grid with spacing $\Delta x = 0.1$ and 24 000 grid points, covering the spatial range $[-1200, 1200]$. For the results presented below, we use a fixed step size $\Delta t = 0.05$ for time propagation and perform a convergence check by using $\Delta t = 0.025$. We compute the time-dependent current

$$J(t) = \sum_{j,\sigma} \int dx \text{Re} \left[\varphi_{j,\sigma}^*(x, t) \left(-i \frac{\partial}{\partial x} + A(t) \right) \varphi_{j,\sigma}(x, t) \right] \quad (10)$$

and evaluate the HHG spectral intensity as the modulus square of the Fourier-transformed current, i.e.,

$$S(\omega) \propto \left| \int dt J(t) \exp(-i\omega t) \right|^2. \quad (11)$$

Here we do not account for macroscopic propagation effects, which may modify the HHG spectra via absorption and phase mismatch. Such propagation effects, however, can be mitigated by controlling the thickness of target materials [9]. Therefore, we expect our discussion to be valid for a thin target material. Furthermore, note that the coherent radiation would propagate perpendicular to the linear chain and hence nondipole effects resulting from the consideration of the dot product between the propagation vector and the position vector would not be present along the chain due to the orthogonality of these vectors.

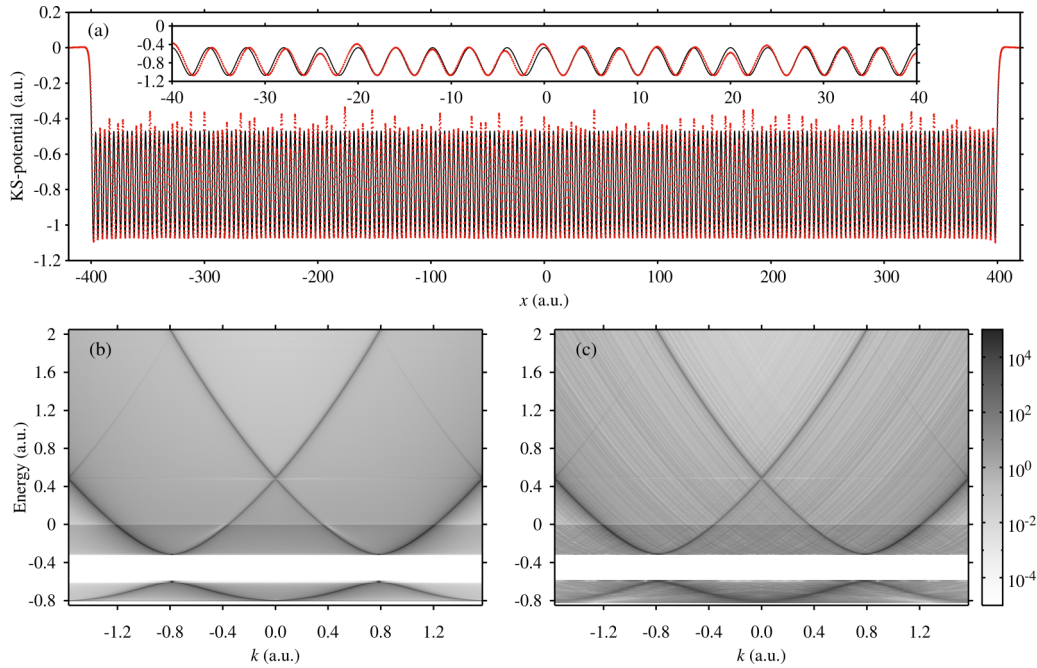


FIG. 1. (a) Comparison of the field-free KS potentials between the model system without disorder (solid black line) and a disordered system with $\delta = 0.4$ [see Eq. (2)] (dotted red line). The inset shows a zoomed-in view of the potentials over 20 unit cells in the center of the model system. Also shown are band structures, which are obtained from the k -space distribution of the KS orbitals, for (b) the disorder-free system and (c) the disordered system considered in (a). The first Brillouin zone boundary is at $k = \pm\pi/a = \pm 0.7854$.

III. RESULTS AND DISCUSSION

A. Disorder-induced changes of field-free properties

We first examine the disorder-induced changes of the field-free properties in the DFT language. Figure 1(a) shows the static KS potentials of the model systems with and without disorder. Remember that our models are large enough to mimic condensed-matter systems [35–37]. Basically, each local minimum of the KS potential corresponds to the position of a nucleus. One can therefore observe the change of the ionic locations from the effective KS potential. For the model system without disorder, the static KS potential shows a periodic multiwell structure, except for the region near the system boundary. One can see that random shifts of the ionic locations disturb the multiwell structure in terms of not only shifting the positions of local extrema, but also resulting in peaks (valleys) of different heights (depths) in the effective potential.

With the static KS potential at hand, one can find the occupied and unoccupied KS orbitals together with their corresponding energies [Eq. (3)] and then use the Fourier-transformed orbitals (in k space) to construct the band structures, as done in Refs. [15,35,36]. The finiteness of the simulation box can lead to the appearance of the free-space parabola $k^2/2$ [35], which does not play any noticeable role for HHG in solids [36]. In the present work we exclude the free-space dispersion from the band structures by introducing a mask function

$$M(x) = \begin{cases} 1, & |x| \leq R_1 \\ \cos^2 \left[\frac{\pi(|x| - R_1)}{2(R_2 - R_1)} \right], & R_1 < |x| < R_2 \\ 0, & |x| \geq R_2 \end{cases} \quad (12)$$

multiplied by the real-space KS orbitals before Fourier transforming to k space. The two parameters R_1 and R_2 in Eq. (12) are chosen such that

$$\frac{\int_{-R_1}^{-R_2} dx n(x) + \int_{R_1}^{R_2} dx n(x)}{\int_{-\infty}^{\infty} dx n(x)} \approx 10^{-6}, \quad (13a)$$

$$\frac{\int_{-R_2}^{-R_1} dx n(x) + \int_{R_2}^{R_1} dx n(x)}{\int_{-\infty}^{\infty} dx n(x)} \approx 10^{-8}, \quad (13b)$$

which approximately define the finite system size according to the electron density, and in the present calculations $R_1 = 402.5$ and $R_2 = 404.5$ are used.

The band structures for the model system without disorder and for the disordered system are shown in Figs. 1(b) and 1(c), respectively. The energy range includes the fully occupied valence band and two conduction bands. For both systems, the band gap (BG) between the valence band and the first conduction band is ~ 0.3 (at $k = \pm\pi/a$), and similar signatures of band structures are clearly observed in the two systems. Meanwhile, we find that the plot in Fig. 1(c) displays more structures than the plot in Fig. 1(b), i.e., a specific energy corresponds to more k values in addition to the band-structure curves, which indicates that the KS orbitals for the disordered model are less localized in k space than those for the system without disorder. This can be understood in view of the fact that in the disordered case, the valleys of different depths in the KS potential [Fig. 1(a)] lead to more localized KS orbitals in real space. We note that the present type of disorder does not introduce any states within the band gap, which is different from the case with disorder introduced in terms of doping-type impurities [15].

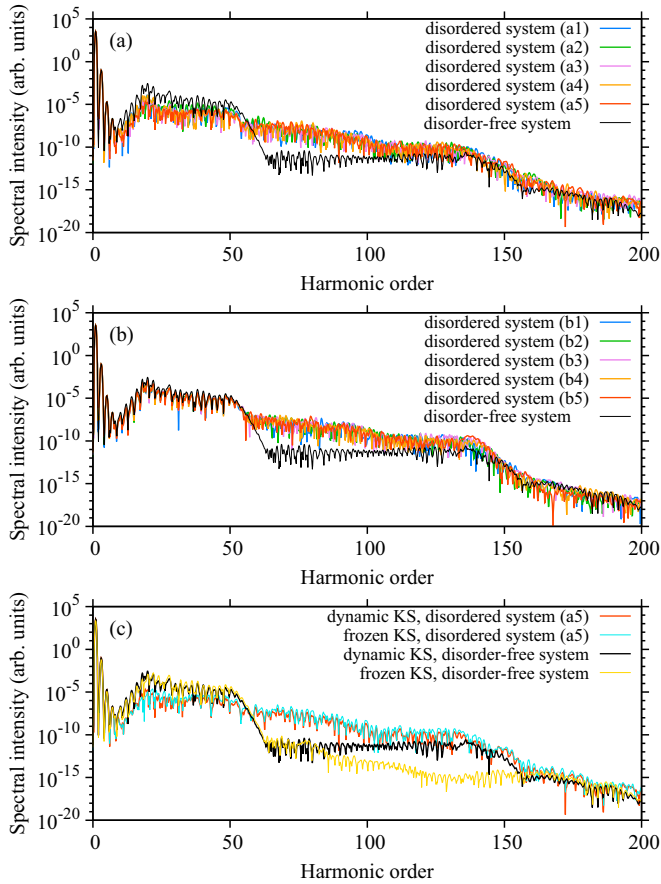


FIG. 2. (a) HHG spectra of representative disordered model systems with $\delta = 0.4$ [Eq. (2)]. (b) Same as (a) but with $\delta = 0.2$. In both (a) and (b) the spectrum of the system without disorder (solid black curve) is shown for comparison. (c) HHG spectra obtained from calculations with the dynamic KS potential and the frozen KS potential (see the text) for a representative disordered system and the disorder-free system. The laser parameters are $A_0 = 0.3$, $\omega_0 = 0.015$, and $N_c = 8$ [Eq. (7)].

Note that the disorder-induced changes of the KS potential and the band structures are obtained self-consistently within the DFT framework. By considering, in our simulations, a set of model systems with different random shifts of the ionic locations [Eq. (2)], we have confirmed that our qualitative findings regarding static KS potentials and band structures are universal for the disordered systems corresponding to imperfect crystals. Indeed, in the following discussion of the disorder-induced changes in HHG spectra, one can clearly observe some common features of the disordered systems in the HHG spectra, from which we draw some general conclusions for HHG in imperfect crystals.

B. Disorder-induced changes of HHG spectra

Having prepared many disordered systems in their ground states using different random shifts of the ionic locations, we perform the corresponding TDDFT simulations [Eq. (8)] and calculate the HHG spectra. The results are presented in Fig. 2 for a fixed laser parameter $A_0 = 0.3$, with the HHG spectrum from the disorder-free system also displayed for comparison.

Before starting the discussion of the HHG spectra, let us first revisit the intra- and interband contributions of HHG in solids [12,13]. Intraband HHG stems from the laser-driven electron motion within band structures with anharmonicity. Typically, the intraband HHG intensity decreases with increasing harmonic order. Interband HHG is described by the generalized three-step model for solids: First an electron tunnels into the conduction band, leaving a hole in the valence band; then the electron and hole move in their respective bands and may recombine at a later time, emitting a photon with energy above the BG energy.

For the considered laser frequency $\omega_0 = 0.015$, which is in the midinfrared regime, harmonics up to order 20 are in the sub-BG regime. With increasing harmonic order, the intensity of intraband HHG decreases and interband HHG becomes dominant when going into the above-BG regime, resulting in a spectral minimum in the sub-BG region (of order ~ 8) and a spectral maximum around the BG energy (of order ~ 20). Such spectral features have also been observed in some other works using different methods [29,43]. For the system without disorder, the HHG spectrum has two plateaus, with their corresponding cutoffs of order ~ 50 and ~ 140 , respectively. Although the mechanisms of the HHG plateaus and cutoffs are not the main focus of this paper, for completeness we would like to briefly mention that the first cutoff can be explained by semiclassical analysis of the electron (hole) motion in the conduction (valence) band [13,20]. Note that for the considered vector-potential amplitude $A_0 = 0.3$, the electron, after tunneling has occurred at $k = \pm\pi/a$, cannot reach the minimum BG between the first and second conduction bands (at $k = 0$). The second plateau and the corresponding cutoff may be related to many-electron effects as discussed in a recent paper [38]. The authors of Ref. [38] proposed a hauling-up effect to explain how the valence-band electrons climb up to the second conduction band and contribute to interband HHG when taking into account correlated-electron dynamics, in principle also included in the present TDDFT approach. In addition to the TDDFT simulations with the time-dependent KS potential [Eq. (9)], we perform calculations with a frozen ground-state KS potential, as done in Refs. [15,35–37,39]. Such a frozen-KS-potential approach is typically applicable when the electron density is not significantly changed during the laser pulse and it captures all the independent-electron dynamics [39]. As will be shown below, the second plateau for the disorder-free system, which is a signature of correlated-electron dynamics [38], cannot be well described within the frozen-KS-potential approach.

As shown in Fig. 2(a), the HHG spectra for the disordered systems with $\delta = 0.4$ manifest some common features. (i) The harmonics below order ~ 8 are of intensity similar to those in the system without disorder, implying that the low-order harmonic signals are not significantly influenced by disorder. (ii) The harmonics of order ~ 8 to ~ 55 , which are dominated by the interband HHG process between the valence band and the first conduction band, have weaker signals than those in the system without disorder. (iii) The harmonics of order ~ 55 to the second cutoff around harmonic ~ 140 are however enhanced when disorder is introduced in the ionic positions. For a smaller displacement of the nuclei with $\delta = 0.2$, as shown in Fig. 2(b), the suppression of the HHG signal in the first plateau

region is less pronounced. This finding is consistent with the results in Ref. [16]. The disorder-induced enhancement of HHG signals in the second plateau region, however, is clearly shown in both Figs. 2(a) and 2(b). Note that in Figs. 2(a) and 2(b), five spectra from randomly selected disordered systems are presented. We have performed TDDFT simulations for a number of randomly generated disordered systems and have confirmed that our findings are indeed of a general nature. The HHG spectra obtained from calculations with the dynamic KS potential and the frozen KS potential are compared in Fig. 2(c). For the system without disorder, the frozen-KS-potential approach is applicable for harmonics below order ~ 75 , while it underestimates the HHG signals in the second plateau region. This confirms that the second plateau stems from correlated-electron dynamics [38], which is beyond the independent-electron picture. For the disordered system, we see from the figure that the frozen-KS-potential approach is generally accurate for all the harmonics. This implies that the disorder-induced enhancement of HHG signals in the second plateau region could be attributed to the independent-electron dynamics, a point we will return to below. We note that all the HHG results presented in this paper, except for Fig. 2(c), are obtained from the full TDDFT simulations with the dynamic KS potential.

To further demonstrate the universality of the observed disorder effects on HHG in the considered midinfrared regime, we calculate HHG spectra at different vector-potential amplitudes for the systems with and without disorder and present the results in Fig. 3. For the disorder-free system [Fig. 3(a)], the first cutoff shows an approximately linear A_0 dependence, which is a well-known feature of HHG in solids. The second plateau is only pronounced for stronger field strengths $A_0 \gtrsim 0.25$, which is qualitatively consistent with the findings in Ref. [38]. One can clearly see from Fig. 3 that the first cutoff is essentially the dividing line between the two parts of the HHG spectra where disorder has the opposite effect on the HHG signals. Indeed, our above findings from Fig. 2 are generally valid for different field strengths: The harmonics are suppressed by disorder in the first plateau region, while the harmonics are enhanced by disorder in the second plateau region.

Note that in the presence of disorder, it is nontrivial to make a semiclassical analysis for the HHG processes, because breaking the lattice periodicity makes the Bloch electron picture inappropriate. To gain some insight into the disorder-induced change of the dynamics in the system, we consider the field-free KS orbitals as a basis set and examine the transition matrix elements of the laser interaction [described by the operator $\hat{p} = -i\frac{\partial}{\partial x}$ in the velocity gauge; see Eq. (8)]. We calculate the transition matrix elements $p_{mn} = \langle \varphi_m | \hat{p} | \varphi_n \rangle \sqrt{\rho_m \rho_n}$, where φ_m and φ_n are the m th and the n th static KS orbitals with the same spin [Eq. (3)] and the spin index is dropped for notational convenience. Here the transition matrix elements are scaled by the density of states ρ_m and ρ_n , since the discretized orbital energies in our finite model are viewed as a series of sampling points in the energy bands. As can be seen in Fig. 4, the amplitudes $|p_{mn}|$ to some extent reflect the laser-driven transitions. The transition matrix elements are closely related to the band structures shown in Figs. 1(b) and 1(c). To illustrate this point, in Fig. 4 we label the initial-state orbital

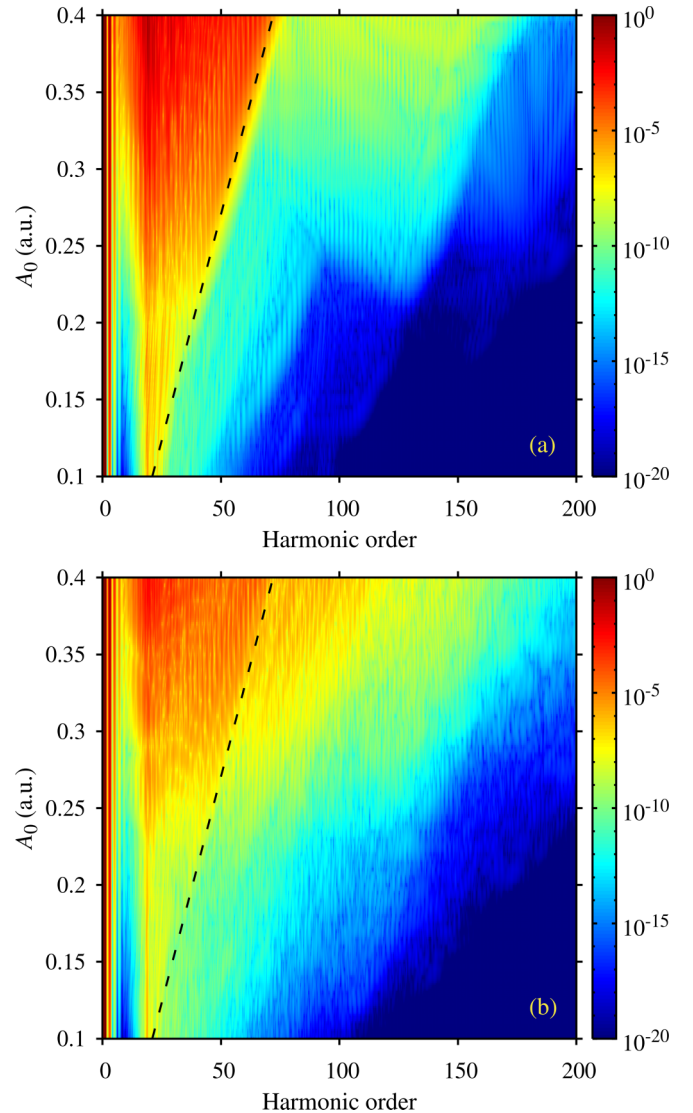


FIG. 3. HHG spectra as a function of vector-potential amplitude A_0 for (a) the system without disorder and (b) a disordered system [the sample system (a5) in Fig. 2]. The dashed lines indicate the first cutoff for the system without disorder. The remaining laser parameters are the same as in Fig. 2.

by its most probable momentum k and the final-state orbital by its orbital energy and present the amplitudes $|p_{mn}|$ for transitions from initial-state orbitals in the first conduction band to final-state orbitals with higher energies. For the disorder-free system, Fig. 4(a) shows that a state with its most probable momentum k is most likely to transit to an adjacent state in the same band or a state with the k -space distribution peaking at an equivalent k value in a different band. This reflects the description of the electron motion in the three-step model for HHG in solids: The electron in k space either adiabatically follows the band structure or makes a vertical transition to another band. For the disordered system, we observe in Fig. 4(b) that in addition to the two above-mentioned types of transitions, there are more transition couplings allowing electrons to climb up in energy without necessarily moving according to the band-structure curve. The disorder-induced change

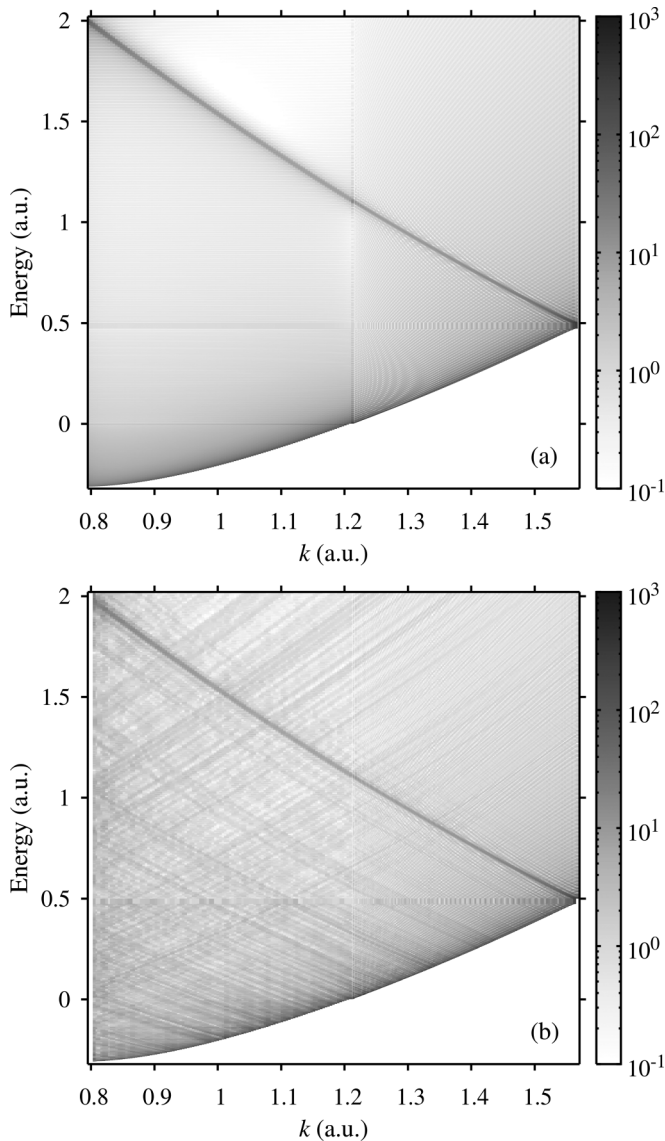


FIG. 4. Norm of the transition matrix elements between field-free KS orbitals for (a) the system without disorder and (b) a disordered system with $\delta = 0.4$ as also shown in Fig. 1. The horizontal axis and the vertical axis indicate the most probable momentum k of the initial-state orbital and the KS orbital energy of the final-state orbital, respectively (see the text). The initial-state orbitals considered in this plot are in the first conduction band, while the corresponding final-state orbitals are in the first and the second conduction bands [see Figs. 1(b) and 1(c)]. For a specific initial-state orbital, transitions to final-state orbitals with higher energies are shown.

of the transition couplings can provide many more resonantly enhanced pathways that enable electrons to more easily reach the second conduction band, resulting in more HHG signals in the second plateau corresponding to the range of energy difference between the second conduction band and the valence band. Note that the discussion of the transition matrix elements is based on the independent-electron picture. In the presence of disorder, the harmonics in the second plateau region are indeed dominated by independent-electron processes, eliminating the feature of correlated-

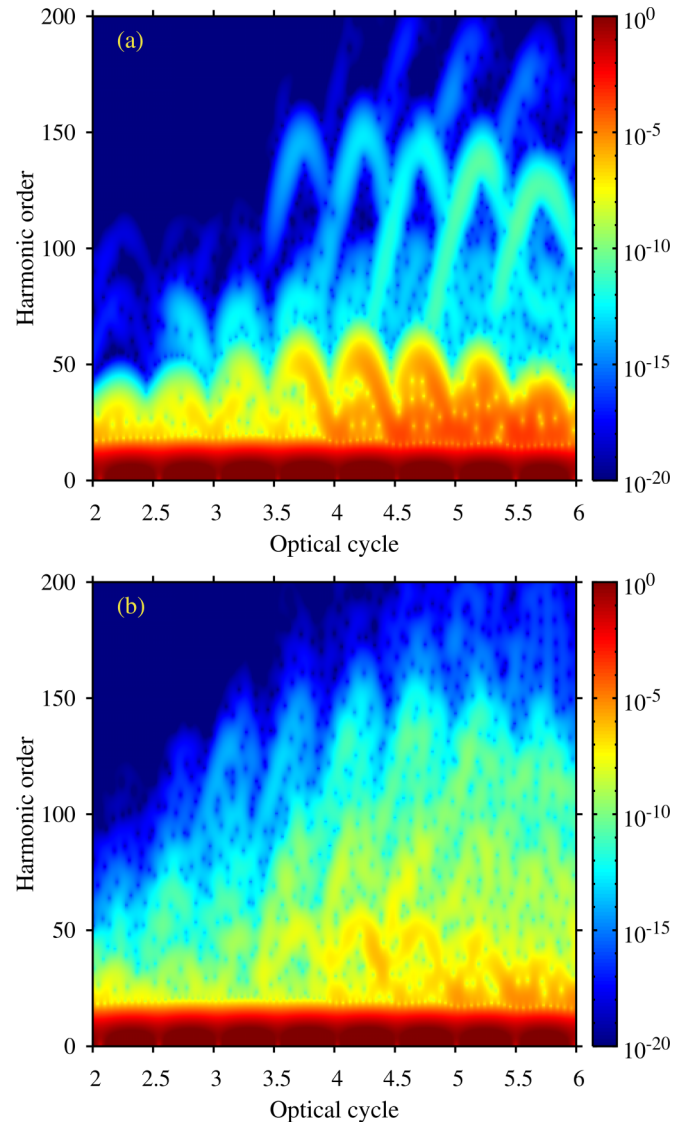


FIG. 5. Time-frequency profile of HHG spectra extracted by a Gabor transform for (a) the disorder-free system and (b) a disordered system [the sample system (a5) in Fig. 2]. The laser parameters are the same as in Fig. 2.

electron dynamics observed in the disorder-free system [see Fig. 2(c)].

A time-frequency profile of HHG spectra is helpful for understanding how the HHG spectra are built up in the time domain [16]. To this end, for the systems with and without disorder, we perform a Gabor transform of the current $J(t)$,

$$G(\omega, t) = \int dt' J(t') \exp(-i\omega t') \exp\left[-\frac{(t-t')^2}{2\tau^2}\right], \quad (14)$$

where the width of the time window τ is chosen to be 5π (a.u.). The Gabor spectra $|G(\omega, t)|^2$ for the disorder-free and a disordered system are compared in Fig. 5. We see that for the system without disorder, the harmonics in both the first and second plateaus show some regular structures in the time domain, which were also observed in Refs. [29,38]. In the disordered case, the emission of harmonics is less regular

in time, which is a feature induced by breaking the lattice periodicity by random shifts of ionic locations.

IV. CONCLUSION

Using a self-consistent TDDFT approach, we have studied HHG in imperfect crystals which are modeled by random shifts of the ionic locations. Compared with the disorder-free system, disordered systems irradiated by midinfrared laser pulses are found to emit suppressed harmonics in the first plateau region and enhanced harmonics in the second plateau region. When decreasing the amplitude of the random displacement of the nuclei, the suppression of harmonics in the first plateau region becomes less pronounced, while the enhancement in the second plateau region remains almost unaffected. The universality of our findings has been demonstrated for many disordered sample systems and for different laser field strengths. The difference between systems with and without disorder was further investigated in terms of the transition matrix elements between the static KS orbitals. Compared with the disorder-free system, a disordered system was found to have more laser-driven transitions among the electronic states. This disorder-induced change is proposed

to account for the increase of the HHG yield in the second plateau region, since the electrons are more likely to reach the second conduction band via richer transitions in the presence of disorder. Finally, a time-frequency profile of HHG spectra showed that the emission of harmonics is less regular in time for a disordered system, which is regarded as a feature of breaking the lattice periodicity by random shifts of ionic positions. Our study constitutes a step forward in the investigation of disorder-induced change of HHG processes in condensed-matter systems and might be relevant to HHG in a thin sample of amorphous materials. Actually, exploring the complicated processes in disordered systems still remains one of the theoretical challenges in this research area. This question, if addressed further in some future works, would allow us to gain a more general and in-depth understanding of HHG in condensed-matter systems.

ACKNOWLEDGMENTS

This work was supported by the Villum Kann Rasmussen Center of Excellence QUSCOPE (Quantum Scale Optical Processes). The numerical results were obtained at the Centre for Scientific Computing, Aarhus.

-
- [1] J. L. Krause, K. J. Schafer, and K. C. Kulander, High-Order Harmonic Generation from Atoms and Ions in the High Intensity Regime, *Phys. Rev. Lett.* **68**, 3535 (1992).
 - [2] A. L'Huillier and P. Balcou, High-Order Harmonic Generation in Rare Gases with a 1-ps 1053-nm Laser, *Phys. Rev. Lett.* **70**, 774 (1993).
 - [3] F. Krausz and M. Ivanov, Attosecond physics, *Rev. Mod. Phys.* **81**, 163 (2009).
 - [4] S. Ghimire, A. D. DiChiara, E. Sistrunk, P. Agostini, L. F. DiMauro, and D. A. Reis, Observation of high-order harmonic generation in a bulk crystal, *Nat. Phys.* **7**, 138 (2011).
 - [5] O. Schubert, M. Hohenleutner, F. Langer, B. Urbanek, C. Lange, U. Huttner, D. Golde, T. Meier, M. Kira, S. W. Koch *et al.*, Sub-cycle control of terahertz high-harmonic generation by dynamical Bloch oscillations, *Nat. Photon.* **8**, 119 (2014).
 - [6] T. T. Luu, M. Garg, S. Y. Kruchinin, A. Moulet, M. T. Hassan, and E. Goulielmakis, Extreme ultraviolet high-harmonic spectroscopy of solids, *Nature (London)* **521**, 498 (2015).
 - [7] G. Vampa, T. Hammond, N. Thiré, B. Schmidt, F. Légaré, C. McDonald, T. Brabec, and P. Corkum, Linking high harmonics from gases and solids, *Nature (London)* **522**, 462 (2015).
 - [8] M. Hohenleutner, F. Langer, O. Schubert, M. Knorr, U. Huttner, S. Koch, M. Kira, and R. Huber, Real-time observation of interfering crystal electrons in high-harmonic generation, *Nature (London)* **523**, 572 (2015).
 - [9] G. Ndashimiye, S. Ghimire, M. Wu, D. A. Browne, K. J. Schafer, M. B. Gaarde, and D. A. Reis, Solid-state harmonics beyond the atomic limit, *Nature (London)* **534**, 520 (2016).
 - [10] S. Y. Kruchinin, F. Krausz, and V. S. Yakovlev, Colloquium: Strong-field phenomena in periodic systems, *Rev. Mod. Phys.* **90**, 021002 (2018).
 - [11] P. B. Corkum, Plasma Perspective on Strong Field Multiphoton Ionization, *Phys. Rev. Lett.* **71**, 1994 (1993).
 - [12] G. Vampa, C. R. McDonald, G. Orlando, D. D. Klug, P. B. Corkum, and T. Brabec, Theoretical Analysis of High-Harmonic Generation in Solids, *Phys. Rev. Lett.* **113**, 073901 (2014).
 - [13] G. Vampa and T. Brabec, Merge of high harmonic generation from gases and solids and its implications for attosecond science, *J. Phys. B* **50**, 083001 (2017).
 - [14] S. Almalki, A. M. Parks, G. Bart, P. B. Corkum, T. Brabec, and C. R. McDonald, High harmonic generation tomography of impurities in solids: Conceptual analysis, *Phys. Rev. B* **98**, 144307 (2018).
 - [15] C. Yu, K. K. Hansen, and L. B. Madsen, Enhanced high-order harmonic generation in donor-doped band-gap materials, *Phys. Rev. A* **99**, 013435 (2019).
 - [16] G. Orlando, C.-M. Wang, T.-S. Ho, and S.-I. Chu, High-order harmonic generation in disordered semiconductors, *J. Opt. Soc. Am. B* **35**, 680 (2018).
 - [17] Y. S. You, Y. Yin, Y. Wu, A. Chew, X. Ren, F. Zhuang, S. Gholam-Mirzaei, M. Chini, Z. Chang, and S. Ghimire, High-harmonic generation in amorphous solids, *Nat. Commun.* **8**, 724 (2017).
 - [18] T. T. Luu and H. J. Wörner, Measurement of the Berry curvature of solids using high-harmonic spectroscopy, *Nat. Commun.* **9**, 916 (2018).
 - [19] T. T. Luu, Z. Yin, A. Jain, T. Gaumnitz, Y. Pertot, J. Ma, and H. J. Wörner, Extreme-ultraviolet high-harmonic generation in liquids, *Nat. Commun.* **9**, 3723 (2018).
 - [20] G. Vampa, C. R. McDonald, G. Orlando, P. B. Corkum, and T. Brabec, Semiclassical analysis of high harmonic generation in bulk crystals, *Phys. Rev. B* **91**, 064302 (2015).
 - [21] C. R. McDonald, G. Vampa, P. B. Corkum, and T. Brabec, Interband Bloch oscillation mechanism for high-harmonic generation in semiconductor crystals, *Phys. Rev. A* **92**, 033845 (2015).

- [22] T. T. Luu and H. J. Wörner, High-order harmonic generation in solids: A unifying approach, *Phys. Rev. B* **94**, 115164 (2016).
- [23] C. R. McDonald, K. S. Amin, S. Aalmalki, and T. Brabec, Enhancing High Harmonic Output in Solids through Quantum Confinement, *Phys. Rev. Lett.* **119**, 183902 (2017).
- [24] P. G. Hawkins, M. Y. Ivanov, and V. S. Yakovlev, Effect of multiple conduction bands on high-harmonic emission from dielectrics, *Phys. Rev. A* **91**, 013405 (2015).
- [25] M. Wu, S. Ghimire, D. A. Reis, K. J. Schafer, and M. B. Gaarde, High-harmonic generation from Bloch electrons in solids, *Phys. Rev. A* **91**, 043839 (2015).
- [26] M. Wu, D. A. Browne, K. J. Schafer, and M. B. Gaarde, Multilevel perspective on high-order harmonic generation in solids, *Phys. Rev. A* **94**, 063403 (2016).
- [27] Z. Guan, X.-X. Zhou, and X.-B. Bian, High-order-harmonic generation from periodic potentials driven by few-cycle laser pulses, *Phys. Rev. A* **93**, 033852 (2016).
- [28] T.-Y. Du, Z. Guan, X.-X. Zhou, and X.-B. Bian, Enhanced high-order harmonic generation from periodic potentials in inhomogeneous laser fields, *Phys. Rev. A* **94**, 023419 (2016).
- [29] T. Ikemachi, Y. Shinohara, T. Sato, J. Yumoto, M. Kuwata-Gonokami, and K. L. Ishikawa, Trajectory analysis of high-order-harmonic generation from periodic crystals, *Phys. Rev. A* **95**, 043416 (2017).
- [30] T.-Y. Du, D. Tang, X.-H. Huang, and X.-B. Bian, Multichannel high-order harmonic generation from solids, *Phys. Rev. A* **97**, 043413 (2018).
- [31] J.-Z. Jin, H. Liang, X.-R. Xiao, M.-X. Wang, S.-G. Chen, X.-Y. Wu, Q. Gong, and L.-Y. Peng, Michelson interferometry of high-order harmonic generation in solids, *J. Phys. B* **51**, 16LT01 (2018).
- [32] T. Otobe, High-harmonic generation in α -quartz by electron-hole recombination, *Phys. Rev. B* **94**, 235152 (2016).
- [33] N. Tancogne-Dejean, O. D. Mücke, F. X. Kärtner, and A. Rubio, Ellipticity dependence of high-harmonic generation in solids originating from coupled intraband and interband dynamics, *Nat. Commun.* **8**, 745 (2017).
- [34] N. Tancogne-Dejean, O. D. Mücke, F. X. Kärtner, and A. Rubio, Impact of the Electronic Band Structure in High-Harmonic Generation Spectra of Solids, *Phys. Rev. Lett.* **118**, 087403 (2017).
- [35] K. K. Hansen, T. Deffge, and D. Bauer, High-order harmonic generation in solid slabs beyond the single-active-electron approximation, *Phys. Rev. A* **96**, 053418 (2017).
- [36] K. K. Hansen, D. Bauer, and L. B. Madsen, Finite-system effects on high-order harmonic generation: From atoms to solids, *Phys. Rev. A* **97**, 043424 (2018).
- [37] D. Bauer and K. K. Hansen, High-Harmonic Generation in Solids with and without Topological Edge States, *Phys. Rev. Lett.* **120**, 177401 (2018).
- [38] T. Ikemachi, Y. Shinohara, T. Sato, J. Yumoto, M. Kuwata-Gonokami, and K. L. Ishikawa, Time-dependent Hartree-Fock study of electron-hole interaction effects on high-order harmonic generation from periodic crystals, *Phys. Rev. A* **98**, 023415 (2018).
- [39] H. Wang, Y. Feng, S. Fu, J. Li, X. Zhang, and H. Du, Complex carrier-envelope-phase effect of solid harmonics under nonadiabatic conditions, *Phys. Rev. A* **99**, 023406 (2019).
- [40] H. Driieke and D. Bauer, Robustness of topologically sensitive harmonic generation in laser-driven linear chains, *Phys. Rev. A* **99**, 053402 (2019).
- [41] *Computational Strong-Field Quantum Dynamics: Intense Light-Matter Interactions*, edited by D. Bauer (De Gruyter, Berlin, 2017).
- [42] C. A. Ullrich, *Time-Dependent Density-Functional Theory: Concepts and Applications* (Oxford University Press, Oxford, 2011).
- [43] S. Aalmalki, A. M. Parks, T. Brabec, and C. R. McDonald, Nanoengineering of strong field processes in solids, *J. Phys. B* **51**, 084001 (2018).